

Lattices with Large Dynamic Aperture for ILC Damping Rings*

A. Wolski[†]

Lawrence Berkeley National Laboratory, Berkeley, CA 94720

(Dated: February 17, 2005)

The ILC damping rings will need a large acceptance to ensure good injection efficiency for the high-emittance, high-power beam from the positron source. The damping rings also need to have very low natural emittance for the collider to reach good luminosity. Meeting the simultaneous requirements for large dynamic aperture and low natural emittance presents a challenge for the lattice design. Previous designs have been based on theoretical minimum emittance cells in the arcs; here, we present two lattice designs using simple FODO cells. The first design is for a 5 GeV ring with 16 km circumference and a layout similar to the TESLA “dogbone” damping ring. The second design is based on the same optics, but the circumference is reduced to 6.3 km by eliminating part of the long straight sections; this results in a small improvement in the dynamic aperture. The shorter ring also operates at the lower energy of 3.74 GeV. A drawback with both designs is that the high dispersion in the arcs leads to a large momentum compaction, which in turn leads to a requirement for a very high RF voltage, and a large value for the synchrotron tune. As well as presenting the designs and an analysis of the dynamic aperture in each lattice, we briefly consider the collective effects and, for the 16 km lattice, discuss the coupling bumps needed to reduce the space-charge tune shift.

I. INTRODUCTION

The basic requirements of the ILC damping rings are that they accept a large beam from the particle sources, and produce a highly stable, low-emittance beam for the downstream systems, at the machine repetition rate of 5 Hz. We base the designs presented in this note on the specifications set out in the TESLA TDR [1]. In the TESLA design, the injected positron beam was expected to have a normalized emittance of 0.01 m (horizontal and vertical), and the normalized emittances of the extracted beam were specified to be $8 \mu\text{m}$ horizontally and $0.02 \mu\text{m}$ vertically. Each bunch train consisted of 2820 bunches with 2×10^{10} particles, and a nominal bunch separation of 337 ns in the main linac. A bunch train of this length must be compressed if the damping rings are to be of a reasonable size. The TESLA TDR specified damping rings of 17 km, with a bunch separation of 20 ns, based on the expected performance of the kickers that would be needed for injecting and extracting bunches individually. A ring with a 6 km circumference has been proposed by Mishra et al [2], using kickers with rise times of 6 ns.

One of the main challenges with any lattice design for the ILC damping rings is achieving a good dynamic aperture. The average injected beam power for a 5 GeV ring will be 226 kW, so loss of even a small fraction of the injected beam can cause large radiation loads in the damping ring. This makes the acceptance of the ring an important issue, and a good dynamic aperture (as well as a large physical aperture) will be essential. Previous lattice designs have usually been based on theoretical minimum

emittance (TME) cells in the arcs, which generally have low dispersion and large chromaticity; this means that strong sextupoles are needed for chromatic correction, and the result is often a limited dynamic aperture. Cai [3] proposed the use of FODO cells in a predamping ring, and recently has discussed the design of a small damping ring using FODO cells. In this note, we report the design of a 16 km lattice using FODO cells in the arcs. The large circumference has the advantage of easing the requirements on the injection and extraction kickers, and possibly of providing more flexibility in operation (for example, if good kicker performance can be achieved, it might be possible to allow a reduction in bunch charge by increasing the number of bunches in the pulse train). There are also some disadvantages to the large circumference, including the need to couple the beam in the long straight sections to reduce the space-charge forces.

Our main concern in the present design has been to achieve a dynamic aperture which is several times the injected beam size over the range of energy deviations expected in the injected beam. We consider only an “ideal” lattice, that is, one without any systematic or random higher-order multipoles in the main magnets, and without any steering errors or tuning errors. In dynamic aperture calculations, we have used a linear model for the damping wiggler, consisting of a sequence of dipole elements. It is known that the systematic nonlinearities in the wiggler field can have a significant impact on the dynamic aperture; however, the precise effects are sensitive to the details of the wiggler design, and it is possible that they may be mitigated by compensating elements. We therefore regard the effects of the damping wiggler on the dynamic aperture as beyond the scope of the present work.

The 16 km lattice has long straight sections designed to be located in the same tunnel as the main linac: this reduces the overall tunnel length needed for the damp-

*This work was supported by the Director, Office of Science, High Energy Physics, U.S. Department of Energy under Contract No. DE-AC03-76SF00098.

[†]Electronic address: awolski@lbl.gov

ing rings. The chromaticity of the long straight sections requires non-local correction in the arcs. This has some impact on the dynamic aperture, and it is interesting to consider the effect of reducing the circumference by eliminating some of the length of the straight sections. This can be achieved rather easily, and we present some results from a version of the lattice with a 6.3 km circumference. Although there is some benefit to the dynamic aperture resulting from a shorter circumference, the gain is fairly small because the long straight sections are designed to have very low chromaticity per unit length.

Designing a lattice with large dispersion in the arcs helps to reduce the strengths of the chromatic sextupoles; however, the large dispersion also leads to a high value for the momentum compaction. In consequence, both lattices presented here have a requirement for a very high RF voltage (115 MV for the 16 km lattice, and 25 MV for the 6.3 km lattice) to achieve a $9 \mu\text{m}$ longitudinal emittance, and the synchrotron tunes are rather large (0.25 for the 16 km lattice, and 0.13 for the 6.3 km lattice). It is possible to reduce the dispersion so as to reduce the RF voltage and synchrotron tune to more acceptable values; however, this will have some impact on the dynamic aperture. Some optimization is needed to find a good balance between these competing effects.

In this note, we begin with a general description of the lattices, and discuss some considerations of the fill pattern, RF system, alignment sensitivities etc. We proceed to present the results of frequency map analysis of the dynamic aperture, and an evaluation of the acceptance using a nominal distribution for an injected positron beam. Finally, we consider some of the collective effects that may have an impact on the operational performance of the damping rings. For the case of the 16 km lattice, we discuss the ‘‘coupling bumps’’ needed in the long straight sections to reduce the space-charge forces.

II. GENERAL LATTICE DESCRIPTION

The main lattice parameters are given in Table I, and the beam parameters are given in Table II. The footprint of the 16 km lattice is shown in Figure 1, and that of the 6.3 km lattice is shown in Figure 2. Each lattice is composed of two arcs, each with circumference roughly 1.4 km, joined by long straight sections. The long straight sections contain the RF cavities and the wiggler, and a series of high-beta FODO cells. In the case of the 16 km lattice, the FODO cells compose most of the length of the straight. Each arc consists of 84 FODO cells. The final 21 cells bend in the reverse direction to the preceding 63 cells, so that a forward bend of 270° is followed by a reverse bend of 90° . The result is that the exit of the arc is parallel to the entrance, but with the beam traveling in the opposite direction. The distance between the entrance and exit beamlines can be controlled by inserting short straight sections of different lengths after 90° and 270° total bending. Matching the dispersion to

zero at either end of the arc is achieved by adjusting the quadrupole strengths in the final three FODO cells. Note that the sextupoles in these cells are omitted, so that sextupoles appear only in the regular, periodic arc cells. The straight sections between the arcs are tuned so that the phase advances horizontally and vertically between the periodic arc cells take on integer values. For on-energy particles, this means that the dynamics in the lattice are essentially determined by the dynamics in one arc cell; this simplifies optimization of the dynamic aperture. For off-energy particles, the phase advances in the straight sections vary because of the chromaticity, resulting in a reduction in dynamic aperture.

The damping wiggler in both the 16 km and the 6.3 km lattices has a total length of 441 m. In the 16 km lattice, the peak field is 1.6 T; this gives a damping time of a little under 27 ms which is sufficient to reduce the injected emittances to the specified extraction values after 200 ms (one machine cycle). At 5 GeV, the damping time in the 6.3 km lattice with 441 m of 1.6 T wiggler would be a little over 10 ms; the significant margin on this damping time allows us to reduce both the beam energy and the wiggler peak field for the same length of wiggler, which has the benefit of reducing both the energy spread and the natural emittance. However, a lower energy does make the beam more sensitive to collective effects. To keep the lattice functions in the 6.3 km lattice the same as those in the 16 km lattice, the wiggler peak field has been reduced in proportion to the energy, to 1.2 T. The beam energy in the 6.3 km lattice is 3.74 GeV, which was chosen to give a damping time of around 27 ms, while avoiding major spin resonances.

The lattice functions at the entrance to one arc, including three periodic arc cells, are shown in Figure 3. The RF cavities are interleaved with sections of the wiggler: the lattice functions in the cavities and wiggler are shown in Figure 4. The lattice functions at the entrance to one long (high-beta) straight section are shown in Figure 5. The coupling bump included in this part of the lattice is discussed in more detail below. For now, we simply note that the lattice functions are defined so that the rms beam sizes are given by:

$$\langle x^2 \rangle = \beta_x \varepsilon_x + \beta_{11}^{\text{II}} \varepsilon_y \quad (1a)$$

$$\langle xy \rangle = \beta_{13}^{\text{I}} \varepsilon_x + \beta_{13}^{\text{II}} \varepsilon_y \quad (1b)$$

$$\langle y^2 \rangle = \beta_{33}^{\text{I}} \varepsilon_x + \beta_y \varepsilon_y \quad (1c)$$

where the transverse emittances are ε_x and ε_y . Using the above equations, it is apparent from Figure 5 that in the case $\varepsilon_y \ll \varepsilon_x$, the beam is approximately round (with some small tilt in the drifts between the quadrupoles).

The lattice functions in one full periodic section of the 6.3 km lattice are shown in Figure 6. Note that there is no coupling in the 6.3 km lattice. The phase advances in one arc cell are a little below 90° horizontally and vertically, and were chosen to give a good dynamic aperture for on-energy particles. The dynamic aperture is not highly sensitive to the exact phase advances, which

TABLE I: General lattice parameters.

Energy	E	5.00 GeV	3.74 GeV
Circumference	C	15935 m	6333.5 m
Harmonic number	h	34550	13732
Revolution frequency	f_0	18.813 kHz	47.334 kHz
RF frequency	f_{RF}	650.0 MHz	650.0 MHz
RF voltage	V_{RF}	115 MV	24.7 MV
Synchronous phase	ϕ_s	80.1°	75.5°
Energy loss per turn	U_0	19.78 MeV	6.191 MeV
Damping times	τ_x, τ_y, τ_z	26.9, 26.9, 13.4 ms	25.5, 25.5, 12.8 ms
Tunes	ν_x, ν_y, ν_s	75.783, 76.413, 0.252	65.783, 66.413, 0.130
Natural chromaticity	ξ_x, ξ_y	-90, -95	-78, -84
Natural transverse emittance	ε_0	0.673 nm	0.377 nm
Momentum compaction	α_p	0.474×10^{-3}	1.19×10^{-3}
Natural bunch length	σ_z	6.38 mm	9.06 mm
Natural energy spread	σ_δ	1.41×10^{-3}	0.993×10^{-3}
Natural longitudinal emittance	ε_z	9.0 μm	9.0 μm

TABLE II: Beam parameters.

Circumference	C	15935 m	6333.5 m
Particles per bunch	N_0	2.0×10^{10}	2.0×10^{10}
Number of bunches	n_b	2826	2808
Bunch spacing	$\Delta\tau_b$	15.38 ns	6.154 ns
Bunches per train	n_{train}	18	36
Bunches per gap		4	8
Number of bunch trains		157	78
Average current	$\langle I \rangle$	170 mA	426 mA
Injected normalized emittance	$\gamma\varepsilon_{\text{inj}}$	0.01 m	0.01 m
Equilibrium vertical emittance	$\gamma\varepsilon_y$	0.02 μm	0.02 μm

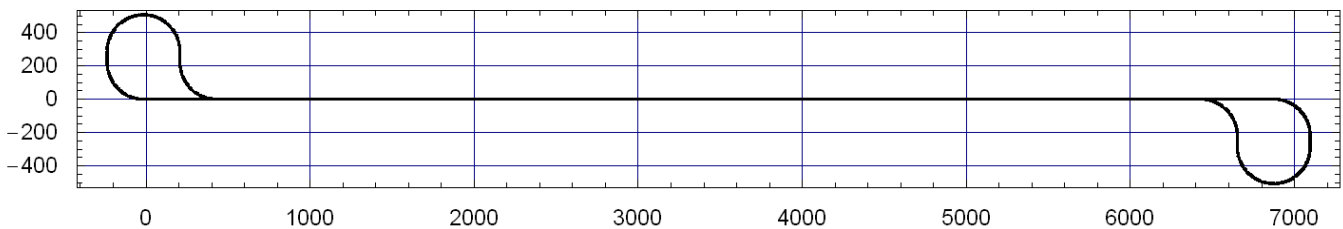


FIG. 1: Footprint of 16 km lattice.

allows some flexibility in controlling the overall tunes of the lattice. As we mentioned above, the straight sections are tuned to give integer phase advances between periodic sections of the arcs. The tunes of the lattice therefore need to be controlled by adjusting the phase advances over the arc cells rather than the straights. Since the arcs in the 16 km and the 6.3 km lattices are the same, the fractional parts of the tunes in the two lattices are the same. The final working point has been chosen with

the following considerations:

- The vertical tune should be close to the half integer, to minimize sensitivity to quadrupole alignment errors. However, the tune should be sufficiently far from the half integer that the lattice is not overly sensitive to focusing errors.
- The working point should be away from major coupling resonances, to reduce sensitivity of the

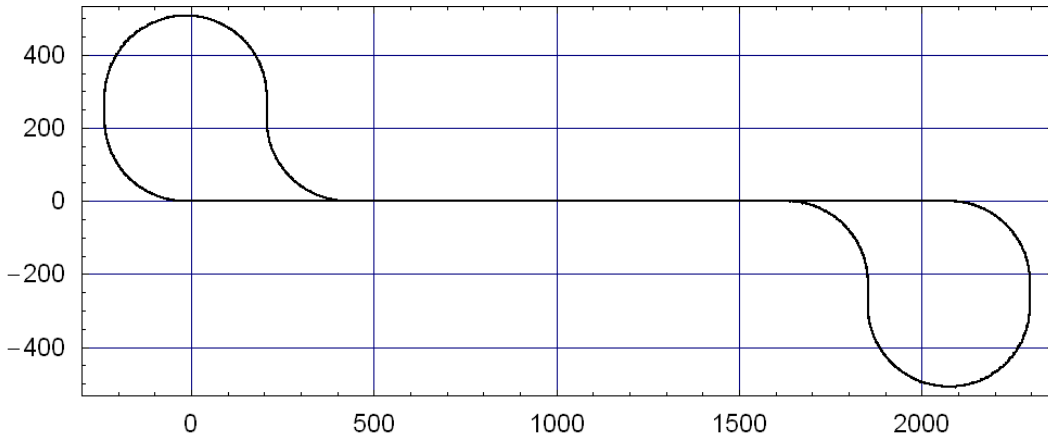


FIG. 2: Footprint of 6.3 km lattice.

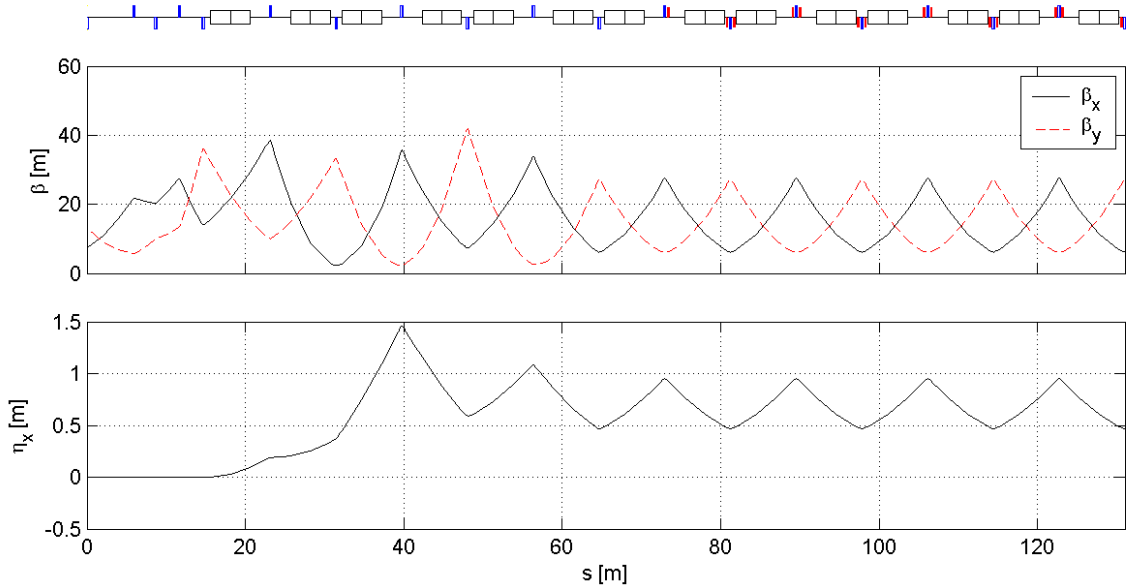


FIG. 3: Beta functions and dispersion at the entrance to one arc, including three periodic FODO cells.

vertical emittance to sextupole misalignment and quadrupole rotation errors.

- The working point should be sufficiently far from major nonlinear resonances, to allow good dynamic aperture.

Ideally, in addition to the above considerations, the horizontal and vertical tunes should also be below the half-integer. Above the half-integer, the coupled-bunch mode most strongly driven by the resistive wall impedance is antidamped; below the half-integer, it is damped. However, the additional requirements on the bunch-by-bunch feedback system from operating slightly above the half-integer, compared to operating slightly below, are not great. In the present case, the vertical tune is below the

half-integer, and the horizontal tune is above the half-integer.

An interesting feature of the 16 km lattice is that the relatively large momentum compaction and the high RF voltage result in some variation in the bunch length and energy spread in different parts of the lattice; in effect, the lattice behaves as a bunch compressor, and the large synchrotron tune is one consequence of this. The variations in bunch length and energy spread may be characterized in terms of longitudinal beta functions, thus:

$$\langle z^2 \rangle = \beta_{55}^{\text{III}} \varepsilon_z \quad (2a)$$

$$\langle z\delta \rangle = \beta_{56}^{\text{III}} \varepsilon_z \quad (2b)$$

$$\langle \delta^2 \rangle = \beta_{66}^{\text{III}} \varepsilon_z \quad (2c)$$

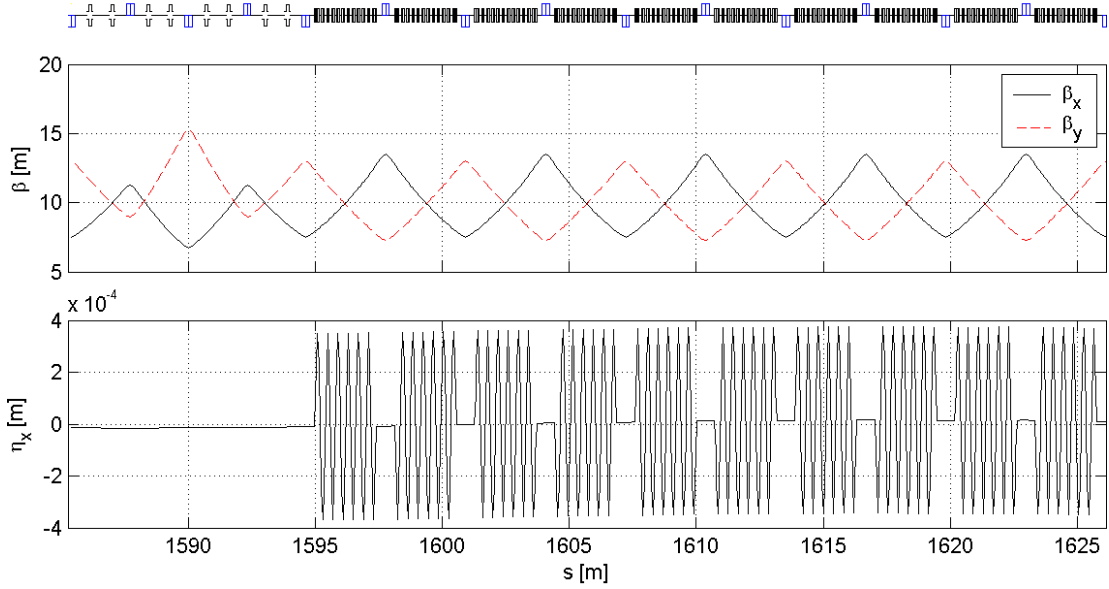


FIG. 4: Beta functions and dispersion in the RF cavities and wiggler.

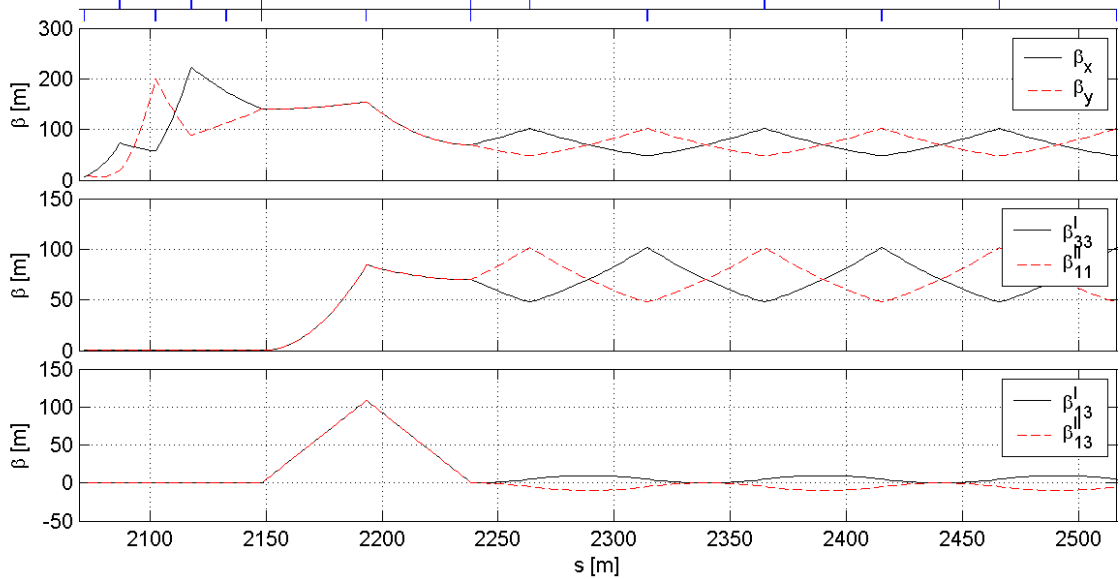


FIG. 5: Beta functions at the entrance to one long straight section.

We have assumed that the transverse emittances are not coupled into the longitudinal plane. The longitudinal beta functions in the 16 km lattice are plotted in Figure 7. The variation of β_{55}^{III} indicates a variation in bunch length of roughly 9% between the maximum and minimum values. We also note that through most of the lattice, there is some correlation between energy deviation and longitudinal position in the bunch. Under these conditions, care is needed when calculating the equilibrium beam distribution; the usual formulae using the syn-

chrotron radiation integrals assume the energy deviation is not correlated with position, and a more general technique, such as Chao's method, must be used. There are similar variations in the bunch length and energy spread in the 6.3 km lattice, but of much smaller amplitude: for this case, the range of variation of the bunch length is a little over 2%.

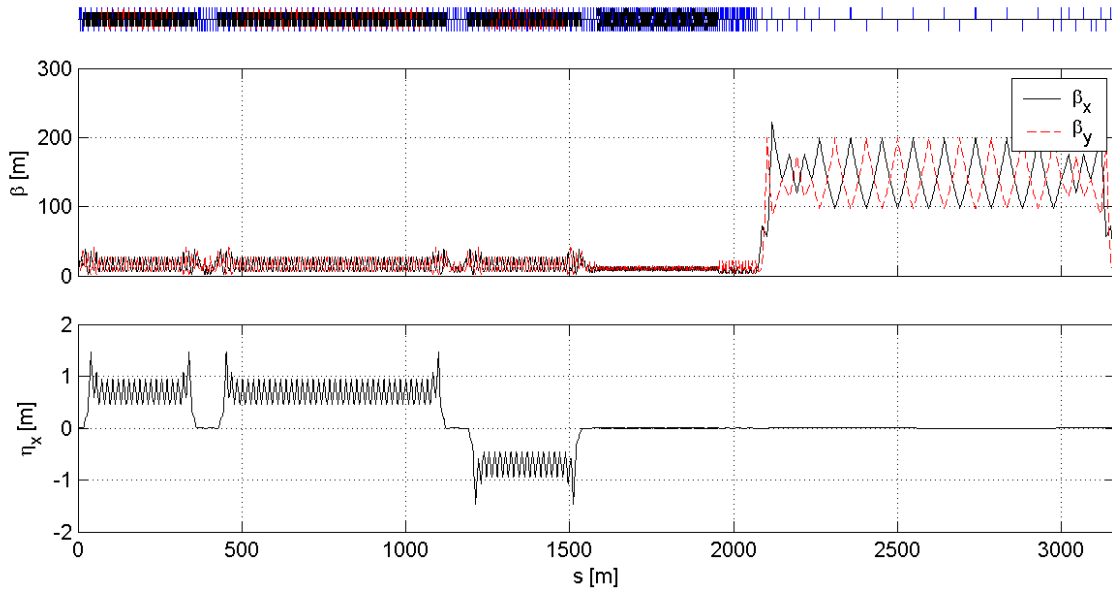


FIG. 6: Beta functions in one half of the 6.3 km lattice.

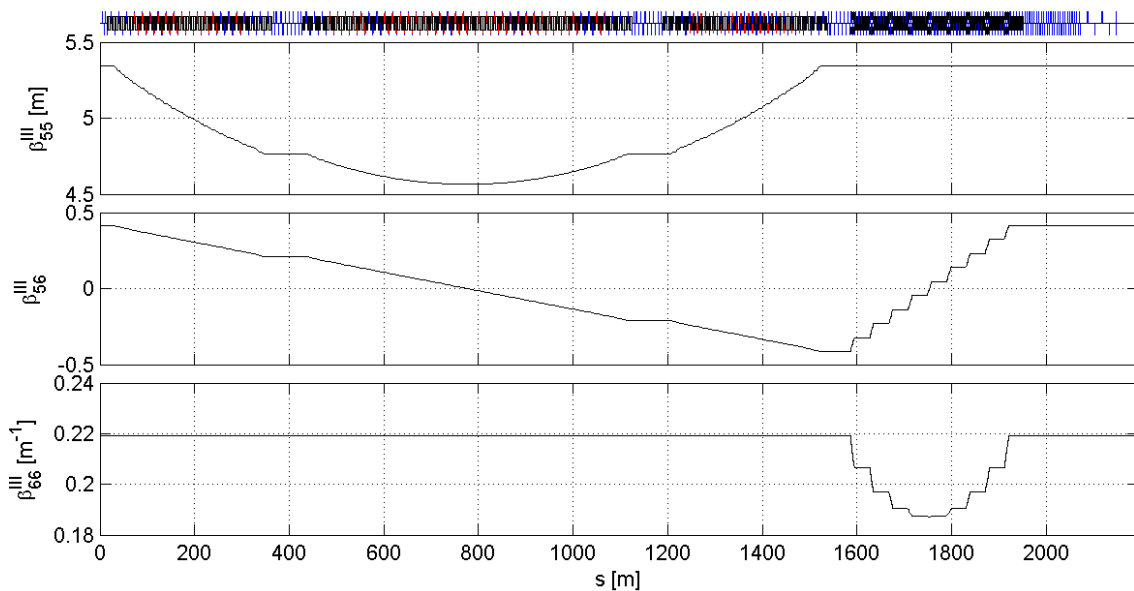


FIG. 7: Longitudinal beta functions in one arc and RF/wiggler section of the 16 km lattice.

III. TECHNICAL SUBSYSTEMS

Here, we outline the general requirements and specifications for the injection/extraction system, the RF system, the multipole magnets and damping wiggler, and the vacuum system.

A. Injection/Extraction Timing and RF System

In each lattice, the bunches are arranged in trains with regular short gaps intended to prevent ion trapping. Extraction proceeds with the last bunch in each train; the gap after the last bunch train is one bunch longer than the others, so that after the last bunch has been extracted from each train, extraction continues with the last-but-one bunch in each train with no delay in the arrival of bunches at the linac. This fixes the harmonic number of

the ring; the frequency of the RF system is then determined by the circumference. In both the 16 km and the 6.3 km lattices, the exact circumference has been chosen so that the RF frequency is 650 MHz, or one half of the main linac RF frequency. With the fill pattern shown in Table II, the time between extracted bunches in the 16 km lattice is 338 ns, very close to the value specified for TESLA. In the 6.3 km lattice, the time between extracted bunches is 271 ns. This may be too short for the linac; an alternative fill pattern could be used, but this would require changing the circumference of the lattice.

The RF voltage in each lattice is chosen to give a longitudinal emittance of $9 \mu\text{m}$. The lower energy spread in the 6.3 km lattice (a result of the lower energy) means that the bunch length is proportionately longer: 9.1 mm, compared to 6.4 mm in the 16 km lattice. The RF voltage in the 16 km lattice is rather large at 115 MV; the 6.3 km lattice needs a more reasonable (but still large) 24.7 MV. A consequence of the large voltage and momentum compaction in each lattice is that the synchrotron tunes are also large, 0.252 and 0.130 in the 16 km and 6.3 km lattices respectively. This may be a concern for synchro-betatron coupling.

B. Dipoles, Quadrupoles, Sextupoles

The parameters of the dipoles and higher multipoles in the 16 km, 5 GeV ring are shown in Table III. We have assumed a full aperture of 60 mm for all magnets, which will allow a vacuum chamber inside radius of 25 mm. this gives a reasonable pole-tip field for all magnets. There is sufficient room in the lattice to allow flexibility in the lengths of the magnets, to increase the aperture while reducing the pole-tip field if necessary. Note that at present, all magnets of a given type have the same length and aperture. For the 6.3 km, 3.74 GeV ring, the magnet strengths are reduced in proportion to the energy.

TABLE III: Parameters of dipoles and strongest multipoles in the 16 km, 5 GeV ring. The aperture is the diameter of the largest circle that can be inscribed between the poles.

Type	Length [m]	Field or Gradient	Aperture [m]	Pole-tip field [T]
Dipoles	4.998	0.1248 T	0.06	0.1248
Quadrupoles	0.30	22.0 T/m	0.06	0.660
Sextupoles	0.20	41.7 T/m ²	0.06	0.0188

C. Damping Wiggler

The wiggler parameters for the 16 km, 5 GeV ring are given in Table IV. The parameters for the 6.3 km, 3.74 GeV ring are the same, except that the peak field is reduced in proportion to the energy, to 1.2 T. Note that

the ends of the wiggler are designed so that the orbit is centered on the wiggler axis; the length of each wiggler section is therefore not exactly the period length multiplied by the given number of periods per section. It is desirable to have as large a physical aperture as possible in the wiggler; this is constrained by the field strength requirements, and the values for the peak field and the period are fairly conservative. A hard-edged dipole model is used at present in the lattice. A magnetic model exists for the 1.6 T wiggler, but design work is needed for a 1.2 T wiggler.

TABLE IV: Wiggler parameters in the 16 km, 5 GeV ring.

Period	λ_w	400 mm
Peak field	\hat{B}_w	1.60 T
Periods per wiggler		6.5
Total number of wigglers		180
Total length of wiggler		441 m

D. Vacuum System

Some parameters of the vacuum system are needed for estimates of certain collective effects. We assume the parameters given in Table V. The circular cross-section is an approximation for purposes of estimates of resistive-wall effects. In the 16 km lattice, the average beam-pipe radius is 32.9 mm, and in the 6.3 km lattice, the average radius is 22.0 mm. The challenging specification on the residual gas pressure (0.1 ntorr) is driven by the ion effects, and will probably require an antechamber.

TABLE V: Vacuum system parameters.

Vacuum chamber material		aluminum
Beam pipe conductivity	σ_c	$3.8 \times 10^7 \Omega^{-1} \text{m}^{-1}$
Vacuum chamber cross-section		circular
Beam-pipe radius in arcs		20 mm
Beam-pipe radius in wiggler		8 mm
Beam-pipe radius in long straight		49 mm
Residual gas pressure	p_0	0.1 ntorr

IV. SINGLE-PARTICLE BEAM DYNAMICS

The principal beam dynamics issues are: the coupling bumps needed to increase the vertical beam size to reduce the space-charge effects in the 16 km lattice; the sensitivity of the vertical emittance to magnet alignment; the dynamic aperture; the impact of various collective effects. We consider each of these issues in turn.

A. Coupling Bumps

Coupling the beam in the straight sections was proposed as a technique to reduce the space-charge forces in the TESLA TDR damping ring design [1]. Without the coupling, the space-charge tune shift was estimated to be around 0.23; the coupling in the straight sections reduced this to 0.035. In principle, implementation of the coupling is straightforward, and the required transformation can be achieved using three skew quadrupoles. The basic concepts have been analyzed and described by Derbenev et al, see for example [4]. Let us consider a point in the beamline where the Twiss beta functions are equal in the horizontal and vertical planes, $\beta_x = \beta_y = \beta$. Also, the Twiss alpha functions are zero and there is no coupling. The beam correlation matrix (sigma matrix) is given by:

$$\Sigma = \begin{pmatrix} \beta\varepsilon_x & 0 & 0 & 0 \\ 0 & \frac{\varepsilon_x}{\beta} & 0 & 0 \\ 0 & 0 & \beta\varepsilon_y & 0 \\ 0 & 0 & 0 & \frac{\varepsilon_y}{\beta} \end{pmatrix} \quad (3)$$

Now we take a symplectic transformation \mathbf{M} :

$$\mathbf{M} = \tilde{\mathbf{R}}\left(-\frac{\pi}{4}\right) \cdot \mathbf{R}(\beta, \mu) \cdot \tilde{\mathbf{R}}\left(\frac{\pi}{4}\right) \quad (4)$$

where $\tilde{\mathbf{R}}$ represents a rotation in co-ordinate space:

$$\tilde{\mathbf{R}}(\theta) = \begin{pmatrix} \cos\theta & 0 & \sin\theta & 0 \\ 0 & \cos\theta & 0 & \sin\theta \\ -\sin\theta & 0 & \cos\theta & 0 \\ 0 & -\sin\theta & 0 & \cos\theta \end{pmatrix} \quad (5)$$

and \mathbf{R} represents a linear transformation in phase space (with different phase advances in the horizontal and vertical planes):

$$\mathbf{R}(\beta, \mu) = \begin{pmatrix} \cos\mu & \beta\sin\mu & 0 & 0 \\ -\frac{1}{\beta}\sin\mu & \cos\mu & 0 & 0 \\ 0 & 0 & -\sin\mu & \beta\cos\mu \\ 0 & 0 & -\frac{1}{\beta}\cos\mu & -\sin\mu \end{pmatrix} \quad (6)$$

After the transformation \mathbf{M} for any value of the phase advance μ , the sigma matrix becomes:

$$\begin{aligned} \Sigma' &= \mathbf{M} \cdot \Sigma \cdot \mathbf{M}^T \\ &= \begin{pmatrix} \frac{1}{2}\beta\varepsilon_+ & 0 & 0 & \frac{1}{2}\varepsilon_- \\ 0 & \frac{1}{2\beta}\varepsilon_+ & -\frac{1}{2}\varepsilon_- & 0 \\ 0 & -\frac{1}{2}\varepsilon_- & \frac{1}{2}\beta\varepsilon_+ & 0 \\ \frac{1}{2}\varepsilon_- & 0 & 0 & \frac{1}{2\beta}\varepsilon_+ \end{pmatrix} \end{aligned} \quad (7)$$

where $\varepsilon_{\pm} = \varepsilon_x \pm \varepsilon_y$. After the transformation, the horizontal and vertical beam sizes are equal, and the beam has no tilt. The required transformation can be achieved using a set of three equally-spaced skew quadrupoles.

The central skew quadrupole needs integrated normalized strength k_1L ; the outer two skew quadrupoles need integrated normalized strengths αk_1L ; the distance between the skew quadrupoles should be d :

$$k_1L = \frac{2\sqrt{2}}{\beta} \quad (8a)$$

$$\alpha = -\frac{1}{2} \left(1 + \frac{1}{\sqrt{2}}\right) \quad (8b)$$

$$d = \frac{\beta}{2\sqrt{1 + \sqrt{2}}} \quad (8c)$$

The same transformation can be used to decouple the beam, as long as the phase advances of the two transverse modes are equal between the transformations. In the 16 km lattice, the coupling is implemented at the entrance to the long straight section, where a matching section is used to set the beta functions to 140 m, and the alpha functions to zero. There does appear to be some sensitivity to the tuning of the coupling bumps; variations in the integrated strengths or distances between the skew quadrupoles can result in a beam that has equal projected beam sizes, but still appears as a flattened ellipse in co-ordinate space. The most effective suppression of the space-charge forces is achieved by making the beam truly round. In the present lattice deck, the coupling transformations are implemented using thin multipoles, with the exact strengths and separations given by equations (8). The resulting lattice functions can be seen in Figure 5: note that the skew quadrupoles are located at 2148 m, 2193 m and 2238 m.

It is convenient for some purposes to be able to turn the coupling off. This is readily achieved by interleaving five normal quadrupoles within the three skew quadrupoles. To couple the beam in the straights, the skew quadrupoles are turned on, and the normal quadrupoles are turned off; to operate without coupling, the skew quadrupoles are turned off, and the normal quadrupoles are turned on. Some adjustment is made to the strengths of quadrupoles in the straight section between the wiggler and the matching to the high-beta part of the straight, to ensure the correct lattice tunes under both conditions.

B. Alignment Sensitivity

The minimum vertical emittance that can be achieved is determined by the vertical opening angle of the synchrotron radiation [5]:

$$\varepsilon_y = \frac{13 C_q}{55 J_y} \frac{\oint \frac{\beta_y}{|\rho|^3} ds}{\oint \frac{1}{\rho^2} ds} \quad (9)$$

For both 16 km and 6.3 km lattices, the minimum vertical emittance (not normalized) is 0.08 pm, or roughly 4% of the specified operating vertical emittance.

The dominant contribution to the vertical emittance will come from magnet misalignments. An equilibrium vertical normalized emittance of $0.02 \mu\text{m}$ is a challenging goal that will require precise magnet alignment and correction of the vertical dispersion and betatron coupling. The sensitivity of the vertical orbit, dispersion and coupling to magnet motion are relevant quantities, which depend on the magnet strengths and lattice functions. To quantify the sensitivities, it is convenient first to define the following quantities:

$$\Sigma_{1O} = \sum_{\text{quadrupoles}} \beta_y(k_1L)^2 \quad (10a)$$

$$\Sigma_{1D} = \sum_{\text{quadrupoles}} \beta_y \eta_x^2(k_1L)^2 \quad (10b)$$

$$\Sigma_{1C} = \sum_{\text{quadrupoles}} \beta_x \beta_y(k_1L)^2 \quad (10c)$$

$$\Sigma_{2D} = \sum_{\text{sextupoles}} \beta_y \eta_x^2(k_2L)^2 \quad (10d)$$

$$\Sigma_{2C} = \sum_{\text{sextupoles}} \beta_x \beta_y(k_2L)^2 \quad (10e)$$

The numeric subscript on the Σ_{**} indicates whether the summation is performed over the quadrupoles or the sextupoles, and the alphabetic subscript identifies the quantity as relevant for the orbit (O), dispersion (D), or betatron coupling (C). The k_1L are the integrated normalized quadrupole strengths, and the k_2L are the integrated normalized sextupole strengths.

In terms of the above quantities, we can write the following approximate relationships:

$$\frac{\langle y^2 \rangle}{\langle \sigma_y^2 \rangle} \simeq \frac{\langle \Delta Y_q^2 \rangle}{8 \varepsilon_y \sin^2 \pi \nu_y} \Sigma_{1O} \quad (11)$$

$$\frac{\varepsilon_y}{\langle \Delta \Theta_q^2 \rangle} \simeq \frac{J_x}{J_y} \frac{1 - \cos 2\pi \nu_x \cos 2\pi \nu_y}{(\cos 2\pi \nu_x - \cos 2\pi \nu_y)^2} \varepsilon_x \Sigma_{1C} + J_\epsilon \frac{\sigma_\delta^2}{\sin^2 \pi \nu_y} \Sigma_{1D} \quad (12)$$

$$\frac{\varepsilon_y}{\langle \Delta Y_s^2 \rangle} \simeq \frac{J_x}{J_y} \frac{1 - \cos 2\pi \nu_x \cos 2\pi \nu_y}{4 (\cos 2\pi \nu_x - \cos 2\pi \nu_y)^2} \varepsilon_x \Sigma_{2C} + J_\epsilon \frac{\sigma_\delta^2}{4 \sin^2 \pi \nu_y} \Sigma_{2D} \quad (13)$$

Here, $\langle y^2 \rangle$ is the mean square vertical orbit distortion; $\langle \Delta Y_q^2 \rangle$ is the mean square vertical quadrupole misalignment; $\langle \Delta Y_s^2 \rangle$ is the mean square vertical sextupole misalignment; $\langle \Delta \Theta_q^2 \rangle$ is the mean square quadrupole rotation about the beam axis; J_x , J_y and J_ϵ are the damping partition numbers; ν_x and ν_y are the betatron tunes, and σ_δ is the rms natural energy spread. These expressions assume that the misalignments are random and uncorrelated, that the betatron coupling is dominated by the lowest-order difference resonance, and that the dispersion in the dipoles and wigglers is not correlated. These assumptions are not necessarily valid for damping rings.

In particular, when calculating the contribution of the vertical dispersion to the emittance, it is important to consider the dispersion in the wiggler separately from the rest of the lattice. This is because the radiation from the wiggler dominates over the radiation from the dipoles. Also, the above expressions do not include the effects of the coupling bump in the 16 km lattice. The emittance tuning is best studied by detailed simulations; however, it is often found that these simple analytical estimates do give a good indication of the sensitivity of the lattice to various misalignments, so we will proceed to evaluate the sensitivity for our 16 km and 6.3 km lattices. In the case of the 16 km lattice, the coupling in the long straight is turned off.

We define the following three measures of the lattice sensitivity:

Quadrupole jitter sensitivity is the rms quadrupole misalignment that will generate an orbit distortion equal to the beam size for a specified emittance. This is found from Eq. (11).

Quadrupole rotation sensitivity is the rms quadrupole rotation that will generate a specified vertical emittance. This is found from Eq. (12).

Sextupole alignment sensitivity is the rms sextupole vertical misalignment that will generate a specified vertical emittance. This is found from Eq. (13).

The values of these sensitivities for the present lattices are given in Table VI. The values for the 16 km lattice are typical for a large storage ring operating with an emittance ratio of around 0.3%. The 6.3 km lattice is less sensitive to misalignments, for two reasons: first, there is a smaller number of magnets in the lattice; and second, under the specified operating conditions, the emittance ratio is larger, close to 0.7%.

TABLE VI: Lattice sensitivities.

Lattice circumference	15935 m	6333.5 m
Quadrupole jitter	273 nm	309 nm
Quadrupole rotation	145 μrad	227 μrad
Sextupole alignment	97.4 μm	169 μm

C. Chromaticity

In both the 16 km and the 6.3 km lattices, the sextupoles in the arcs are tuned to give zero first-order chromaticity. The remaining tune-shifts with energy are second-order and higher. The tune-shifts with energy in the 16 km lattice (with coupling in the long straights) are shown in Figure 8, and the tune-shifts with energy in the 6.3 km lattice are shown in Figure 9.

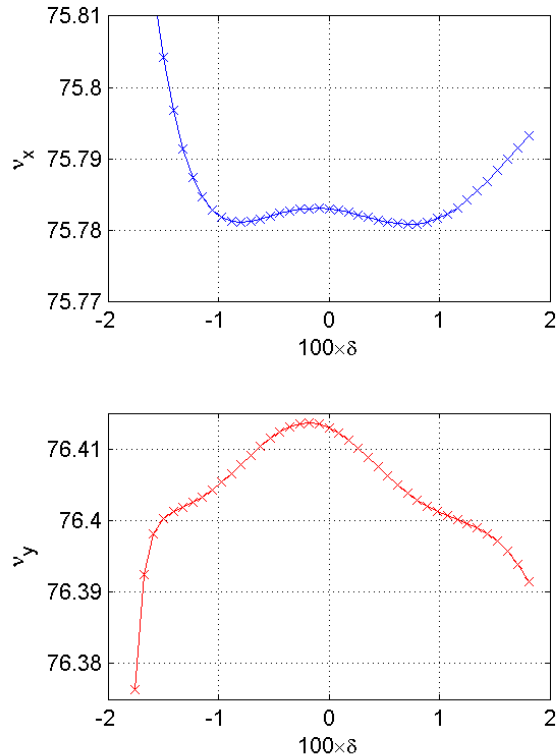


FIG. 8: Tune-shifts with energy in the 16 km lattice.

D. Dynamic Aperture

Achieving a good dynamic aperture was a primary concern in the design of the lattices described here. We attempted to minimize the chromaticity of each section within each lattice, to reduce the sextupole strengths needed for chromatic correction. The arcs were designed with large dispersion and lattice functions at the sextupoles, again to reduce the strengths needed for chromatic correction. Each arc cell was tuned for phase advances that gave good dynamics, and sections between arc cells were tuned for phase advances of an integer $\times 2\pi$, so that the dynamics of on-energy particles the lattice are essentially determined by the dynamics in a single arc cell.

We use frequency map analysis to study the dynamic aperture (see, for example, [6, 7, 8]). The frequency map for on-energy and off-energy dynamics in the 16 km lattice are shown in Figures 10 and 11 respectively. Corresponding plots for the 6.3 km lattice are shown in Figures 12 and 13. Assuming an injected normalized emittance of 0.01 m, the injected rms beam sizes at the observation point are $\sigma_x = 2.77\text{mm}$, $\sigma_y = 3.65\text{mm}$ for the 16 km lattice, and $\sigma_x = 3.20\text{mm}$, $\sigma_y = 4.21\text{mm}$; the on-energy dynamic aperture is around 20σ horizontally, and rather more than 20σ vertically. However, the dynamic aperture

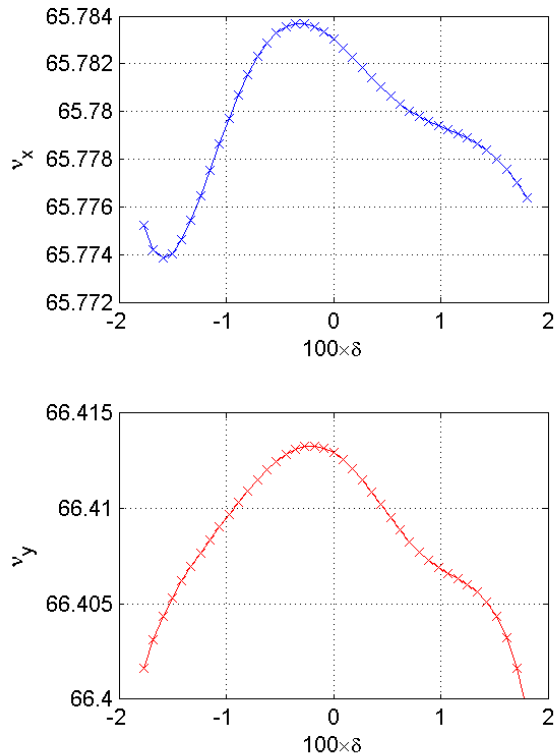


FIG. 9: Tune-shifts with energy in the 6.3 km lattice.

drops rapidly for even small energy deviations, and 10σ seems a more reasonable characterization. The dynamic energy acceptance is rather better in the shorter lattice. This is not surprising, since the additional chromaticity in the long straight sections of the 16 km lattice has an adverse effect on the off-energy dynamics.

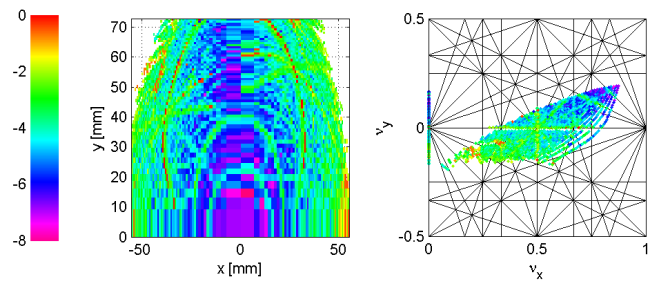


FIG. 10: Frequency map for on-energy dynamics in the 16 km lattice. The lattice functions at the observation point are $\beta_x = 7.5\text{m}$, $\beta_y = 13.0\text{m}$, $\alpha_x = \alpha_y = 0$. The color scale indicates the rate of change of the betatron tunes over the time of the tracking, expressed as $\log_{10} \sqrt{\Delta\nu_x^2 + \Delta\nu_y^2}$ where $\Delta\nu_x$ and $\Delta\nu_y$ are the changes in the tunes between the first 128 turns and the second 128 turns of tracking.

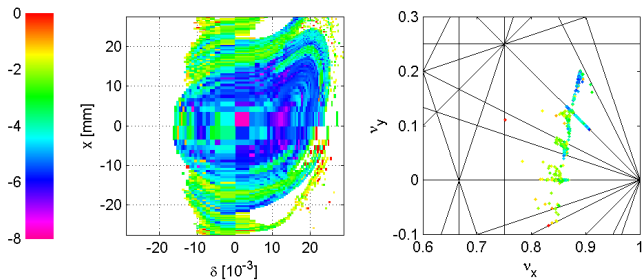


FIG. 11: Frequency map for off-energy dynamics in the 16 km lattice.

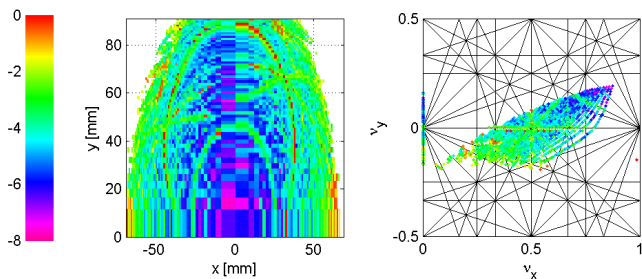


FIG. 12: Frequency map for on-energy dynamics in the 6.3 km lattice. The lattice functions at the observation point are $\beta_x = 7.5\text{m}$, $\beta_y = 13.0\text{m}$, $\alpha_x = \alpha_y = 0$.

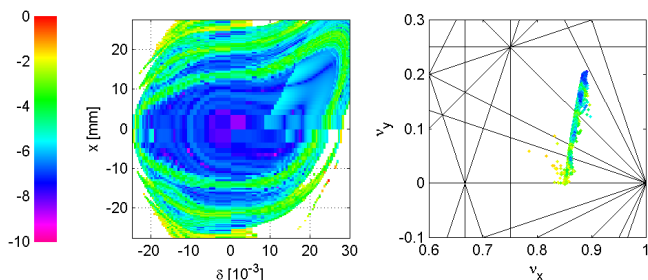


FIG. 13: Frequency map for off-energy dynamics in the 6.3 km lattice.

E. Tracking with Synchrotron Oscillations

The characterization of the dynamic aperture using frequency map analysis does not include the effects of synchrotron oscillations; the plots in Figures 11 and 13 were produced with the RF turned off. To test the full dynamic acceptance, we tracked a sample particle distribution produced by Batygin [9] from modeling of an undulator-based positron source for ILC. In the distribution provided, the transverse normalized emittances are a little over 0.005 m, somewhat smaller than the nominal value of 0.01 m assumed for the damping ring design. However, there are significant tails in the distribution. A set of 1960 particles were tracked through the 16 km

lattice without errors, and with the RF turned on. There was a nominal physical aperture of 1 m applied through the lattice, so all particle losses were the result of the dynamical effects of the sextupoles. Tracking with synchrotron radiation is possible, but no radiation effects were included in this simulation. After 500 turns (equal to one damping time), 15 of the original particles were lost, representing a little under 1% of the injected beam. This would result in a radiation power load of around 20 kW; once errors are included in the lattice, the number of lost particles could be significantly larger. Although the frequency map analysis suggests significant margin in the dynamic aperture for the injected beam, the dynamic aperture is still not sufficient to ensure 100% injection efficiency. Most of the lost particles have large energy errors, which suggests that the limitation lies in the energy acceptance of the lattice. It may be possible to improve the injection efficiency by collimating the positron beam at low energy, shortly after the production target: this remains to be studied.

V. COLLECTIVE EFFECTS

In this section, we present the results of initial estimates of the severity of a variety of collective effects expected to be important. Many of the phenomena we consider need a more careful analysis than we have carried out at the present time; the results here should be interpreted only as general indications of the severity of the relevant effects. For the 16 km lattice, the calculations have been done in most cases with the coupling bumps turned off; for the space-charge tune shift calculations, however, we consider both cases, i.e. with and without coupling in the long straights. We also neglect the variation in bunch length around the ring that we noted in Section II.

A. Microwave and CSR Instability

The Keill-Schnell-Boussard criterion gives an impedance threshold for the longitudinal microwave instability that may be written:

$$\frac{Z_{\parallel}}{n} = Z_0 \sqrt{\frac{\pi}{2}} \frac{\gamma \alpha_p \sigma_{\delta}^2 \sigma_z}{N_0 r_e} \quad (14)$$

where Z_0 is the free-space impedance, γ the relativistic factor, and r_e the classical electron radius. There is also a transverse coasting-beam instability associated with the transverse impedance. Again applying the Keill-Schnell-Boussard criterion, the threshold for this instability may be written:

$$Z_{\perp} = Z_0 \frac{\gamma \alpha_p \sigma_{\delta} \nu_y \omega_0 \sigma_z}{N_0 r_e c} \quad (15)$$

Although the relationship is strictly true only for the resistive wall impedance, the transverse broad-band im-

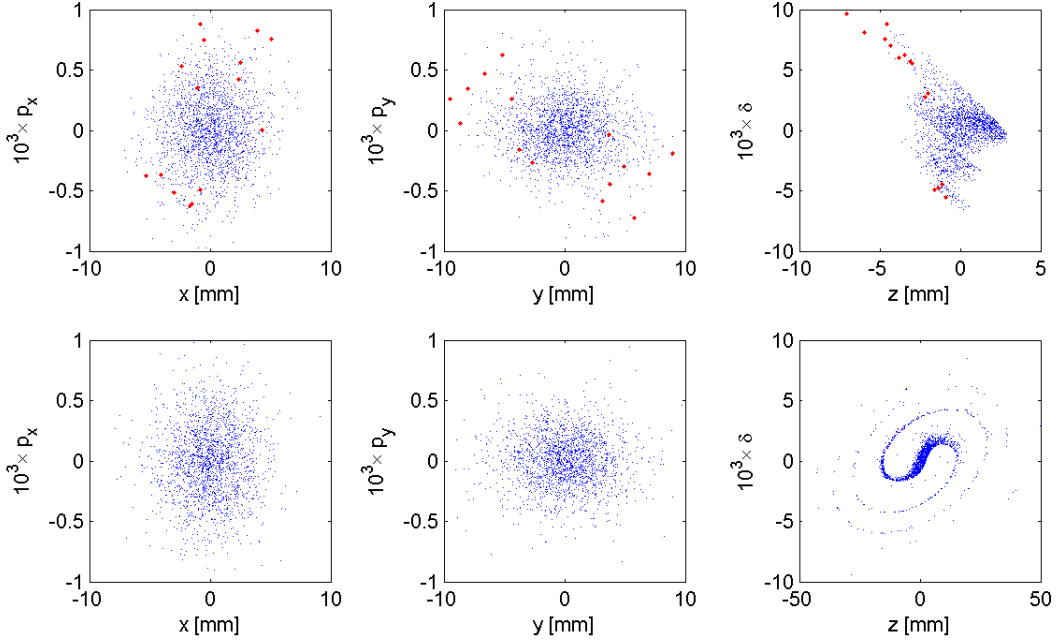


FIG. 14: Phase space of a nominal positron distribution before tracking (top) and after tracking (bottom) 500 turns through the 16 km lattice. The red points in the top plots identify particles that were lost during the tracking.

pedance is often assumed to be related to the longitudinal broad-band impedance through:

$$Z_{\perp} = \frac{2c}{\omega_0 \langle b \rangle^2} \frac{Z_{\parallel}}{n} \quad (16)$$

where $\langle b \rangle$ is the mean vacuum chamber radius.

Coherent synchrotron radiation is also able to drive beam instabilities; the threshold is given as a bunch charge above which, the CSR instability starts to have an effect [10]:

$$N_{0,th} = 3.6 \frac{C}{4\pi \langle b \rangle} \frac{\gamma \alpha_p \sigma_{\delta}^2 \sigma_z}{r_e} \quad (17)$$

Using appropriate values for the parameters, we can evaluate all the above thresholds. The results are given in Table VII.

B. Space-Charge Tune Shift

Space-charge forces lead to a significant vertical tune shift, because of the large circumference and small vertical beam size. In a lattice without betatron coupling, the incoherent tune shift is given by:

$$\Delta\nu_y = -\frac{N_0 r_e}{\sqrt{2\pi^3} \gamma^3 \sigma_z} \int_0^C \frac{\beta_y}{\sigma_y (\sigma_x + \sigma_y)} ds \quad (18)$$

Venturini has generalized this expression to include betatron coupling [11]. The result is:

$$\Delta\nu_k = -\frac{1}{4\pi} \int_0^C \beta_{11}^k F_{xx} + 2\beta_{13}^k F_{xy} + \beta_{33}^k F_{yy} ds \quad (19)$$

where the lattice functions are as defined in Equations 1, with $\beta_{11}^I \equiv \beta_x$ and $\beta_{33}^{II} \equiv \beta_y$. $k(=I,II)$ specifies the transverse mode. The components of the force are given by:

$$F_{xx} = \frac{K}{\sigma_+} \left(\frac{\cos^2 \theta}{\sigma_{\xi}} + \frac{\sin^2 \theta}{\sigma_{\eta}} \right) \quad (20a)$$

$$F_{xy} = \frac{K \sin 2\theta}{2\sigma_+} \left(\frac{1}{\sigma_{\xi}} + \frac{1}{\sigma_{\eta}} \right) \quad (20b)$$

$$F_{yy} = \frac{K}{\sigma_+} \left(\frac{\sin^2 \theta}{\sigma_{\xi}} + \frac{\cos^2 \theta}{\sigma_{\eta}} \right) \quad (20c)$$

where

$$K = \frac{2\lambda r_e}{\beta^2 \gamma^3} \quad (21)$$

θ is the beam tilt, σ_{ξ} and σ_{η} are the major and minor axes of the beam ellipse in co-ordinate space, $\sigma_+ = \sigma_{\xi} + \sigma_{\eta}$, λ is the line density of charge in the bunch, r_e is the classical radius of the electron, β is the normalized velocity of the bunch, and γ the relativistic factor.

The calculated space-charge tune shifts are given in Table VIII. The coupling bumps in the 16 km lattice are effective in reducing the tune shifts to tolerable values.

TABLE VII: Microwave and CSR instability thresholds.

Lattice circumference	C	15935 m	6333.5 m
Longitudinal broad-band impedance threshold	Z_{\parallel}/n	422 m Ω	627 m Ω
Transverse broad-band impedance threshold	Z_{\perp}	19.4 M Ω /m	23.7 M Ω /m
Longitudinal equivalent impedance threshold	$\omega_0 \langle b \rangle^2 Z_{\perp} / 2c$	4139 m Ω	5686 m Ω
CSR instability charge threshold	$N_{0,\text{th}}$	2.5×10^{12}	2.2×10^{12}

The vertical tune shift in the 6.3 km lattice is large compared with that in the coupled 16 km lattice, because of the lower energy. The results are consistent with the relative beam energies, given that the coupled straights make negligible contribution to the space-charge tune shifts. It is possible that the large tune shift in the 6.3 km lattice could have adverse effects on the beam dynamics, and tracking simulations will be needed to study this in more detail.

TABLE VIII: Incoherent space-charge tune shifts.

Lattice	15935 m uncoupled	15935 m coupled	6333.5 m
$\Delta\nu_x$	-0.011	-0.011	-0.0091
$\Delta\nu_y$	-0.21	-0.041	-0.12

C. Resistive-Wall Instability

The resistive-wall impedance of the vacuum chamber will drive a transverse coupled-bunch instability. The impedance is given by:

$$Z_{\perp}(\omega) = (1 - \text{sgn}(\omega) i) Z_0 \frac{C}{2\pi \langle b \rangle^3} \delta_{\text{skin}}(\omega) \quad (22)$$

where the skin depth is:

$$\delta_{\text{skin}} = \sqrt{\frac{2}{\sigma_c \mu_c \omega}} \quad (23)$$

σ_c and μ_c are the conductivity and magnetic permeability of the vacuum chamber. Assuming a uniform fill of n_b bunches with average current $\langle I \rangle$, the growth rate of a transverse mode with mode number m is given by:

$$\frac{1}{\tau_m} = -\frac{c \langle I \rangle}{4\pi \nu_y E / e} \text{Re} \sum_{p=-\infty}^{\infty} Z_{\perp}((\nu_y + n_b p + m) \omega_0) \quad (24)$$

With the nominal operating conditions, the ring will not be uniformly filled, but there will be gaps between bunch trains. We can still estimate the growth rates by assuming a uniform fill, but either using the same average current as in the case where there are gaps between bunch trains, or using the same bunch charge. Using

the same average current will likely underestimate the growth rates; using the same bunch charge will likely overestimate the growth rates. In the present case, the gaps account for roughly 22% of the circumference in both the 16 km lattice and the 6.3 km lattice, so the difference between using the nominal average current and using the nominal bunch charge is not large.

Figure 15 shows the growth rates of the unstable modes in the 6.3 km lattice in the vertical plane, assuming a uniform fill. The red (upper) points show the growth rates with the same charge per bunch as the nominal case; the black (lower) points show the growth rates with the same average current as the nominal case. The blue broken line shows the vertical damping time. Table IX gives the growth times of the instability. A bunch-by-bunch feedback system will be needed to suppress the instability; a potential concern is the jitter induced on the beam by the feedback system.

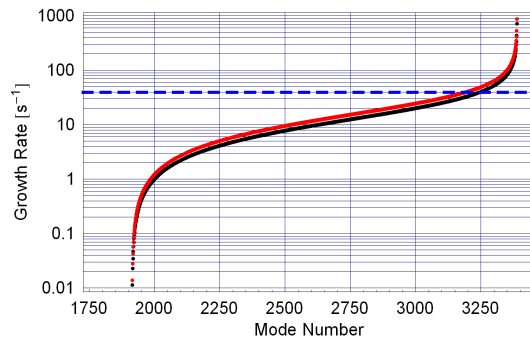


FIG. 15: Growth rates of unstable resistive-wall modes.

TABLE IX: Resistive wall instability growth times, assuming uniform fill at nominal bunch charge.

Lattice circumference	15935 m	6333.5 m
Shortest growth time	2.25 ms	1.15 ms
Shortest growth time	42.3 turns	54.4 turns

We note that higher-order modes in the RF cavities can also drive coupled-bunch instabilities. The RF cavity design is not known at the present time, so we have not investigated these growth rates.

D. Ion Effects

First, we consider ion trapping. Without gaps in the fill, ions with a relative molecular mass greater than $A_{x(y)}$ will be trapped horizontally (vertically), where

$$A_{x(y)} = \frac{N_0 r_p c \Delta \tau_b}{2 \sigma_{x(y)} (\sigma_x + \sigma_y)} \quad (25)$$

At the equilibrium beam size, all ions will be trapped horizontally in both the 16 km and the 6.3 km lattices. In the vertical plane, ions with a relative molecular mass greater than 7 will be trapped in the 6.3 km lattice, and ions with a relative molecular mass greater than 10 will be trapped in the uncoupled 16 km lattice. For both lattices, other ions will be trapped vertically as the beam damps from its injected size. In the coupled 16 km lattice, the larger vertical beam size in the long straight will mean that all ions will be trapped at the equilibrium beam sizes.

It is hoped that the gaps in the fill (77 ns in the 16 km lattice, and 55 ns in the 6.3 km lattice) will be sufficient to clear ions accumulated during the passage of a bunch train. However, we must then consider the fast-ion instability arising from the ions accumulated during one bunch train [12]. The line density of ions at the end of a bunch train is given by:

$$\lambda_{\text{ion}} = N_0 n_{\text{train}} \frac{p_0}{kT} \sigma_{\text{ion}} \quad (26)$$

where σ_{ion} is the ionization cross-section, assumed to be 2 Mb. The presence of the ions causes coherent and incoherent tune shifts, with the incoherent tune shift twice as large as the coherent. Because of the small vertical beam size, the effects are much stronger in the vertical plane. The incoherent vertical tune shift is given by:

$$\Delta \nu_y = \frac{1}{2\pi} \int_0^C K_y \beta_y ds \quad (27)$$

where the ion focusing is given by:

$$K_y = \frac{\lambda_{\text{ion}} r_e}{\gamma \sigma_y (\sigma_x + \sigma_y)} \quad (28)$$

As well as the tune shifts, there is a growth in betatron oscillations of bunches towards the rear of the bunch train, driven by oscillations of the ions in the potential of the beam. The ion oscillation frequency is ω_{ion} , given by:

$$\frac{\omega_{\text{ion}}^2}{c^2} = \frac{\bar{\lambda}_e r_p}{A \sigma_y (\sigma_x + \sigma_y)} \quad (29)$$

where $\bar{\lambda}_e = N_0/c\Delta\tau_b$ is the mean line density of electrons in the beam, A is the relative molecular mass of the residual gas ions in the chamber, and r_p is the classical radius of the proton. The growth rate of betatron oscillations of bunches towards the rear of the bunch train is given by:

$$\frac{1}{\tau} = \frac{f_0}{4\sqrt{2}\sigma_\omega} \int_0^C \omega_{\text{ion}} K_y \beta_y ds \quad (30)$$

where f_0 is the revolution frequency, and σ_ω is the standard deviation of the ion oscillation frequency around the ring, resulting from the variation in beam size.

Table X gives the parameters of the fast-ion instability, found by applying the above expressions to the uncoupled 16 km lattice and the 6.3 km lattice. We assume that the dominant gas species in the chamber is CO. At 0.1 ntorr residual gas pressure, the incoherent tune shift should be small enough in both lattices not to limit operational performance. The exponential growth time is fast, but it may be possible to suppress the instability using a bunch-by-bunch feedback system; as with the resistive wall instability, the concern is the jitter that such a feedback system could induce on the beam. Emittance growth will be associated with the coherent bunch oscillations driven by the accumulated ions. The simple estimates used here indicate that ion effects are likely to be an issue in the damping rings. Further studies, including simulations and experimental work, will be needed to predict the impact on machine performance with more confidence.

E. Electron Cloud Effects

Electrons accumulating in the positron damping ring may have a multitude of dynamical effects on the beam, including single bunch and coupled bunch instabilities. Here, we consider only the single bunch effects. We treat the electron cloud as a broad-band transverse impedance, with resonant frequency characteristic of the oscillation frequency of the electrons in the potential of a single positron bunch. This frequency ω_{cloud} is given by:

$$\frac{\omega_{\text{cloud}}^2}{c^2} = \frac{N_0 r_e}{\sqrt{2\pi} \sigma_z \sigma_y (\sigma_x + \sigma_y)} \quad (31)$$

For both the 16 km and the 6.3 km lattices, the oscillation frequency is large compared to the bunch length (see Table XI), so it is appropriate to use a coasting-beam model for the instability. Following Ohmi and Zimmermann [13], we estimate the transverse impedance from the electron cloud as:

$$Z_\perp = Z_0 C \frac{\hat{\rho}_{\text{cloud}}}{2\lambda_{\text{beam}}} \quad (32)$$

where $\hat{\rho}_{\text{cloud}}$ is the peak cloud density in the beam, and $\lambda_{\text{beam}} = N_0/\sqrt{2\pi}\sigma_z$ is the peak line density of charge in the beam. Using the Keil-Schnell-Boussard criterion, the instability threshold is:

$$Z_{\perp,th} = Z_0 \frac{\gamma \alpha_p \sigma_\delta \nu_y}{N_0 r_e} \frac{\omega_{\text{cloud}} \sigma_z}{c} \quad (33)$$

Combining equations (32) and (33) gives the electron cloud density threshold at which instability occurs:

$$\hat{\rho}_{\text{cloud}} = \sqrt{\frac{2}{\pi}} \frac{\gamma \alpha_p \sigma_\delta \nu_y}{r_e} \frac{\omega_{\text{cloud}}}{cC} \quad (34)$$

TABLE X: Parameters of the fast-ion instability.

Lattice circumference	C	15935 m	6333.5 m
Residual vacuum pressure	p_0	0.1 ntorr	0.1 ntorr
Molecular mass of residual gas (species)	A	28 (CO)	28 (CO)
Ion density at end of bunch train	λ_{ion}	2320 m^{-1}	4635 m^{-1}
Incoherent vertical tune shift	$\Delta\nu_y$	0.038	0.033
Exponential growth time	τ	$745 \mu\text{s}$	$316 \mu\text{s}$
Exponential growth time		14.0 turns	14.9 turns

This may be compared with the mean density of electrons in the chamber expected from the neutralization condition:

$$\rho_{\text{neut}} = \frac{N_0}{\pi \langle b \rangle^2 c \Delta \tau_b} \quad (35)$$

Values are given in Table XI. For both the 16 km and the 6.3 km lattices, the instability threshold appears somewhat higher than the neutralization density. However, the neutralization density is an average density that does not include the enhancement that can occur during a bunch passage. Simulations suggest that the density of the cloud in the bunch can be increased by an order of magnitude during a bunch passage. In this case, an instability will occur. It appears that it will be necessary for both lattices to reduce the density of the cloud in the chamber at least by two orders of magnitude below the neutralization level to prevent an instability.

F. Touschek Lifetime

The beam store time is around 200 ms, which is much less than the Touschek lifetime. However, a reasonable Touschek lifetime is desirable for commissioning and tuning. For flat beams that are non-relativistic in the beam rest frame, and assuming that the energy aperture is given by the RF acceptance δ_{max} , the Touschek lifetime τ is given by [14]:

$$\frac{1}{\tau} = \frac{r_e^2 c N_0}{8\pi \gamma^2 \delta_{max}^3 \sigma_z} \frac{1}{C} \int_0^C \frac{D(\epsilon)}{\sigma_x \sigma_y} ds \quad (36)$$

where the function $D(\epsilon)$ is defined by:

$$\begin{aligned} \frac{D(\epsilon)}{\sqrt{\epsilon}} &= -\frac{3}{2} e^{-\epsilon} + \frac{\epsilon}{2} \int_{\epsilon}^{\infty} \frac{\ln u}{u} e^{-u} du \\ &+ \frac{1}{2} (3\epsilon - \epsilon \ln \epsilon + 2) \int_{\epsilon}^{\infty} \frac{e^{-u}}{u} du \end{aligned} \quad (37)$$

and the argument ϵ is given by:

$$\epsilon = \left(\frac{\delta_{max} \beta_x}{\gamma \sigma_x} \right)^2 \quad (38)$$

Assuming an energy acceptance of 1%, the Touschek lifetime is 52 minutes for the uncoupled 16 km lattice, and

17 minutes for the 6.3 km lattice. An energy acceptance of 1% is likely pessimistic, so the beam lifetime should be reasonable for commissioning and tuning purposes.

G. Intrabeam Scattering

As well as the large-angle scattering leading to particle loss (Touschek effect), particles within a bunch undergo small-angle scattering. The resulting increases in the beam emittances are described by the theory of intrabeam scattering (IBS). To calculate the emittance growth in the present lattice, we use approximate formulae derived by Mtingwa et al [15] to the theory of Bjorken and Mtingwa [16]. This approximation is valid for high-energy beams, and has been shown to be in good agreement to the exact theory in the regime of the damping rings. Calculation of the IBS growth rates involves evaluating complicated integrals (involving the lattice functions and emittances) around the lattice, and the advantage of using the high-energy approximation is that the IBS growth rates can be calculated much more rapidly. This is important, since the growth rates depend on the beam emittances and the equilibrium emittances for a given bunch charge need to be found by iteration. Performing the calculations for the 16 km and the 6.3 km lattices gives the results shown in Table XII. For the case of the 16 km lattice, we have used the version without coupling in the straights. For both the 16 km and the 6.3 km lattices, we have neglected the small variation in the bunch length around the ring. In the uncoupled 16 km lattice, the growth in the horizontal emittance at the nominal bunch charge is not negligible, but the equilibrium horizontal emittance is still within the specified operating value of $8 \mu\text{m}$. The coupling in the long straight should reduce the horizontal emittance growth somewhat, but most of the growth occurs in the arcs, where there is large horizontal dispersion. The growths in the vertical and longitudinal planes are much smaller. In the 6.3 km lattice, the horizontal emittance growth is very much larger: this is a combination of the fact that the natural emittance of the shorter lattice is roughly half that of the 16 km lattice, and the fact that the beam energy in the shorter lattice is lower. Despite the large IBS growth, the equilibrium horizontal emittance in the 6.3

TABLE XI: Parameters of the electron-cloud instability.

Lattice circumference	C	15935 m	6333.5 m
Cloud oscillations per bunch	$\omega_{\text{cloud}}\sigma_z/c$	7.6	12.7
Instability cloud density threshold	$\hat{\rho}_{\text{cloud}}$	$5.3 \times 10^{12} \text{ m}^{-3}$	$13.9 \times 10^{12} \text{ m}^{-3}$
Neutralization density	ρ_{neut}	$1.6 \times 10^{12} \text{ m}^{-3}$	$7.1 \times 10^{12} \text{ m}^{-3}$

TABLE XII: Intrabeam scattering growth rates and emittance growths.

Lattice circumference	C	15935 m	6333.5 m
Bunch charge	N	2×10^{10}	2×10^{10}
Horizontal growth time	T_x	0.203 s	0.0483 s
Vertical growth time	T_y	3.56 s	4.13 s
Longitudinal growth time	T_p	0.976 s	0.345 s
Horizontal emittance growth	$\varepsilon_{x,N}/\varepsilon_x - 1$	15%	110%
Vertical emittance growth	$\varepsilon_{y,N}/\varepsilon_y - 1$	0.8%	0.7%
Energy spread growth	$\sigma_{\delta,N}/\sigma_\delta - 1$	1.5%	3.9%

km lattice (5.8 μm) is still below the specified value of 8 μm . The vertical and longitudinal emittance growths are small, but we should note that in the case that the vertical emittance is generated entirely by betatron coupling (as opposed to vertical dispersion, as we have assumed here), the proportional growth in the vertical emittance will be equal to the proportional growth in the horizontal emittance. This could be an operational concern in the 6.3 km lattice.

VI. COMMENTS AND CONCLUSIONS

A lattice design based on FODO arc cells appears to be a promising approach to achieving a good dynamic aperture in the ILC damping rings. With an appropriate number of arc cells, and a sufficiently long wiggler, it is possible to reach the specification for the natural emittance. Both the 16 km and 6.3 km versions of the lattice presented here use 441 m of wiggler; in the longer lattice, the peak field is 1.6 T, while in the shorter lattice, the peak field is reduced in proportion to the beam energy, to 1.2 T. The lower beam energy in the shorter lattice is helpful in reducing the longitudinal emittance. We should note that since the wiggler is important in achieving the low natural emittance needed in the damping rings, if a design based on FODO cells is considered for the electron damping ring, it will not be possible to reduce the length of wiggler to take advantage of the longer damping time allowed by the smaller injected beam. On the other hand, precisely because the injected electron beam is smaller than the injected positron beam, the requirements for the dynamic aperture are not so challenging, and it will likely be possible to use a design based, for example, on TME cells.

The good dynamic aperture is partly achieved by de-

signing the arc cells for high dispersion; this reduces the strengths of the sextupoles needed for chromatic correction, but has the disadvantage that the momentum compaction factor is very large. As a result, a very high RF voltage is needed to reduce the equilibrium longitudinal emittance to 9 μm , and the synchrotron tune is large. There are possibilities for reducing the momentum compaction factor, including an increase in the number of arc cells. It may be possible to reduce the momentum compaction without reducing the dispersion at the chromatic sextupoles, and thus an adverse impact on the dynamic aperture may be avoided. Also, the large momentum compaction is helpful in raising the thresholds for a variety of collective instabilities, and it is not desirable to reduce it too far. In summary, there are various opportunities for improvement of the lattices presented here, but there are a number of conflicting considerations, and some compromises will be needed.

Even with a dynamic aperture of 10σ of the injected beam for energy errors over $\pm 1\%$, we find a small number of particles lost in a tracking simulation using a nominal injected distribution. The characterization of the dynamic aperture we have used here is not sufficiently detailed to guarantee survival of all particles within a given envelope. It appears likely that to achieve the necessary injection efficiency, it will be necessary to collimate the positron beam more severely (before injection into the damping ring) than was the case in our simulation. The collimation will be done most safely at low energy.

Simple estimates of some of the collective effects suggest that a number of effects will be significant, but the issues of most concern are likely the fast-ion instability, and the electron-cloud effect. It is hoped that appropriate treatment of the vacuum chamber in the positron damping ring will prevent build-up of electron cloud. However, the fast-ion instability appears strong even at the

challenging vacuum pressure of 0.1 ntorr. The coupling bumps in the 16 km lattice appear effective in reducing the space-charge tune shifts, but there is some concern as to the tunability of the optics in the coupling sections.

While the results of analysis of the lattice designs presented here are encouraging, there is a significant amount of further design work to be done. The main priority should be to find an appropriate value for the momentum compaction that reduces the synchrotron tune and the need for a very high RF voltage, while maintaining comfortable levels for instability thresholds. At this stage, there is significant flexibility in adjusting the circumference of the lattice. Although there is some benefit to

the dynamic aperture from reducing the circumference, the effects are not dramatic, and useful design work can be done in advance of a decision for the damping rings' circumference.

Acknowledgements

A FODO lattice for a pre-damping ring was proposed at the ILC Americas Workshop November 2004, by Yunhai Cai (SLAC) whom the author wishes to thank for useful discussions.

-
- [1] TESLA Technical Design Report, DESY 2001-011 (March 2001).
- [2] S. Mishra et al, "Studies Pertaining to a Small Damping Ring for the International Linear Collider," FNAL Report (October 2004).
- [3] Y. Cai, presented at ILC Americas Workshop, SLAC, November 2004.
- [4] A. Burov, S. Nagaitsev, Y. Derbenev, "Circular Modes, Beam Adapters and their Applications in Beam Optics", FERMILAB-Pub-01/060-T (May 2001).
- [5] T.O. Raubenheimer, "The Generation and Acceleration of Low-Emittance Flat Beams for Future Linear Colliders", SLAC-Report-387 (1991).
- [6] C. Steier, D. Robin, L. Nadolski, W. Decking, Y. Wu, J. Laskar, "Measuring and Optimizing the Momentum Aperture in a Particle Accelerator", Phys. Rev. E 65, 056506 (2002).
- [7] D. Robin, C. Steier, J. Laskar, L. Nadolski, "Global Dynamics of the Advanced Light Source Revealed through Experimental Frequency Map Analysis", Phys. Rev. Lett. 85, 558 (2000).
- [8] C. Steier et al, "Lattice Model Calibration and Frequency Map Measurements at the ALS", Proceedings of EPAC 2000, Vienna, Austria.
- [9] Y. Batygin, private communication.
- [10] M. Venturini, "Longitudinal Single-Bunch Instabilities in the NLC Main Damping Ring", LBNL-55103 (May 2004).
- [11] M. Venturini, "First-Order Space-Charge Tune Shift in a Coupled Lattice" (December 2004).
- [12] F. Zimmermann, "Single-Pass Ion Effects in Storage Rings and Linacs", in "Handbook of Accelerator Physics and Engineering" (Edited by A.W. Chao and M. Tigner) pp. 130-131, World Scientific (1999).
- [13] K. Ohmi and F. Zimmermann, "Study of Head-Tail Effect Caused by Electron Cloud", Proceedings of EPAC 2000, Vienna, Austria.
- [14] H. Wiedemann, "Particle Accelerator Physics II" pp. 328-329, Springer (1995).
- [15] K. Kubo, S. Mtingwa and A. Wolski, "Intrabeam Scattering Formulae for High Energy Beams", submitted to Phys. Rev. ST Accel. Beams (October 2004).
- [16] J.D. Bjorken and S.K. Mtingwa, "Intrabeam Scattering", Particle Accelerator **13**, 115 (1983).

Disclaimer

This document was prepared as an account of work sponsored by the United States Government. While this document is believed to contain correct information, neither the United States Government nor any agency thereof, nor The Regents of the University of California, nor any of their employees, makes any warranty, express or implied, or assumes any legal responsibility for the accuracy, completeness, or usefulness of any information, apparatus, product, or process disclosed, or represents that its use would not infringe privately owned rights. Reference herein to any specific commercial product, process, or service by its trade name, trademark, manufacturer, or otherwise, does not necessarily constitute or imply its endorsement, recommendation, or favoring by the United States Government or any agency thereof, or The Regents of the University of California. The views and opinions of authors expressed herein do not necessarily state or reflect those of the United States Government or any agency thereof or The Regents of the University of California.

LBNL is an equal opportunities employer.